

# Tuning Modules With Elastic Instabilities On-the-Fly for Reconfigurable Shapes and Motions

Zhe Chen<sup>ID</sup>, Graduate Student Member, IEEE, Jiefeng Sun<sup>ID</sup>, Member, IEEE,  
and Jianguo Zhao<sup>ID</sup>, Member, IEEE

**Abstract**—Multistable structures, known for their ability to rapidly switch between multiple stable states, are increasingly used for various robotic and mechatronic systems (e.g., grippers, swimming, jumping, or crawling robots). However, existing multistable structures generally have a fixed structure after fabrication, leading to a fixed energy profile with respect to deformations, a concept termed as energy landscape (EL) that dictates a structure's stable configurations and dynamic responses. To overcome this limitation, this work investigates how to actively tune the EL of a beam-based mechanism with a linear spring on the fly to enable tunable modules. We consider two tuning strategies to adjust the beam's initial bending angle and the offset of the spring. We establish a forward model to predict the module's EL and conduct experiments to validate this model. We also address the inverse problem to achieve a desired EL by choosing proper values of the initial bending angle and the offset of the spring. Finally, we demonstrate the practical applications of this tunable module with three cases: A kicker, a configurable arm, and a crawling robot. Our research lays the groundwork for advanced robotic and mechatronic systems, enabling them to harness structures with elastic instabilities for tuning their performance on the fly, thereby enhancing their adaptability and functionality.

**Index Terms**—Bistable, energy landscape, flexible robots, soft robots.

## I. INTRODUCTION

MULTISTABLE structures, characterized by their ability to rapidly switch between multiple stable configurations, represent an emerging area of study in robotic or mechatronic systems. These structures, after switching to a stable state, can maintain the new stable configuration without any external

Manuscript received 20 January 2024; revised 31 March 2024; accepted 30 April 2024. Date of publication 12 June 2024; date of current version 16 August 2024. Recommended by Technical Editor W. Li and Senior Editor Q. Zou. This work was supported in part by National Science Foundation under Grant CMMI-2126039. (Corresponding author: Jianguo Zhao.)

Zhe Chen and Jianguo Zhao are with the Department of Mechanical Engineering, Colorado State University, Fort Collins, CO 80523 USA (e-mail: Jianguo.Zhao@colostate.edu).

Jiefeng Sun is with the School for Engineering of Matter, Transport and Energy, Arizona State University, Tempe, AZ 85287 USA.

This article has supplementary material provided by the authors and color versions of one or more figures available at <https://doi.org/10.1109/TMECH.2024.3402671>.

Digital Object Identifier 10.1109/TMECH.2024.3402671

energy input. A special type of multistable structure is a bistable structure with two stable states, which has been observed widely in nature. For instance, the Venus flytrap's leaves are bistable, which can snap shut in 0.1 s to capture prey [1]. Similarly, the rapid beak closure of hummingbirds is another instance of natural bistability, enabling these birds to catch flying insects efficiently [2].

Inspired by nature's remarkable bistable mechanisms, researchers have recently explored how to leverage multistable or bistable structures to enhance the performance of various systems by exploiting the elastic instability inherent in multistable structures [3], [4]. Comprehensive reviews can be found in [5] and [6], but here, we only review several representative works in this area with a focus on robotic applications. Bistable structures are used to generate fast response [7], enlarged output force [8], [9], and multiple functions [3], [10], [11] for various robotic systems. For instance, Wu et al. [7] developed a bistable thermal actuator with increased actuation speed by harnessing snap-through instability. Inspired by the well-known two-balloons problem, Overvelde et al. [8] exploited the snap-through instability to generate larger motion and higher force with a fluidic actuator. Patel et al. [11] built a bistable module based on a pre-stretched elastomeric membrane and demonstrated three reconfigurable soft robots capable of multimodal locomotion. Other representative examples using bistable mechanisms include swimming robots [12], [13], robotic grippers [14], [15], [16], and robots with jumping capability [17], etc.

For multistable or bistable structures, an important characteristic is the energy landscape (EL): How the stored strain energy varies with respect to the deformation (e.g., bending angle). A typical EL is plotted in Fig. 1(b) as the black curve. The EL can determine both the stable configurations and the dynamic responses of the structures. Despite substantial recent research, existing multistable structures are generally fixed after being fabricated, leading to a predetermined EL [7], [11], constraining their adaptability and application scope.

Addressing this constraint, researchers have recently investigated how varying specific parameters of these structures will influence their ELs, thereby generating different stable configurations or dynamic responses [18], [19], [20]. For instance, our previous work demonstrated a bistable mechanism consisting of a flexible beam curved by a pretensioned spring [21]. Using flexible beams with different initial bending angles, we realized

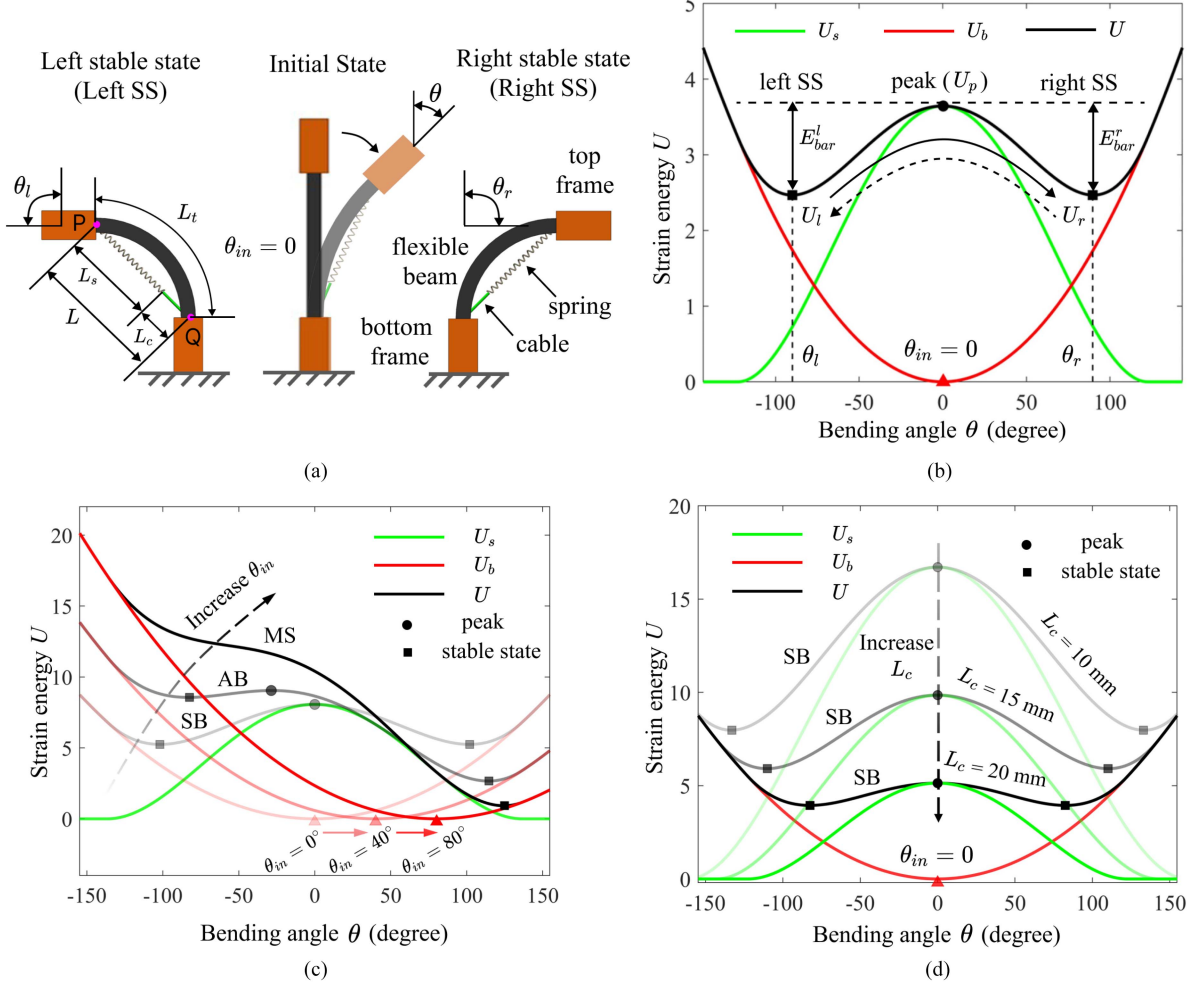


**Fig. 1.** Working principle for tuning the energy landscape (EL) of a beam-based module. (a) A symmetric bistable module in its left stable, straight, and right stable states, respectively. (b) The EL of the symmetric bistable module. (c) When  $\theta_{in}$  increases with  $L_c = 17\text{ mm}$ , the module changes from symmetric to asymmetric bistable and finally to monostable. (d) When  $L_c$  increases with  $\theta_{in} = 0$ , the spring's energy profiles will scale down, changing both the energy barriers and resting angles.

different ELs, including symmetric bistable (SB), asymmetric bistable (AB), and monostable (MS) landscapes. Liu et al. [22] investigated adjusting the EL in a soft gripper, enabling state switching tailored to specific targets. Jiang et al. [23] developed an electroactive soft bistable actuator with adjustable EL by controlling the voltages applied to the twisted and coiled polymer fibers and manually altering the prestretch of the elastic cords. In addition, Pal leveraged magnetic field to adjust the force response and bistability of a magnetoelastomeric beam and applied it to reconfigurable mechanical signal-processing devices [24].

Despite recent progress in adjusting the EL for multistable structures, two issues remain largely unaddressed. First, most of the existing work, with notable exceptions [23], [24], cannot adjust the EL on the fly. Current approaches typically require manual alterations, such as the manual modification of the initial lengths of spring elements [9], [12], [22], or the manual adjustment of the initial bending angle of bistable mechanism by changing the dimension of its bending beam [25], [26]. It would be more advantageous if we could tune the parameters on

the fly to enhance the utility of multistable structures. Second, there are few systematic explorations on how to achieve the desired EL by choosing proper parameters for the multistable structures. Instead, most existing work predominantly conducts simulations or experiments to observe how different parameters will influence the EL [27], [28], [29], [30].

This work presents contributions that directly address these two issues using a beam-based module with a linear spring. The specific contributions are twofold. First, we introduce two strategies to tune the module's EL without manual alterations, adjusting its performance on the fly, such as resting angles and energy barriers. The first strategy employs a shape-morphing beam (SMB) that can bend to and hold a desired angle to adjust the beam's initial bending angle. The second strategy uses an adjustable cable driven by a motor to adjust the offset of the linear spring. The second major contribution of this work lies in our systematic explorations on how to achieve a desired EL by choosing the proper parameters for those two tunable elements. We call this the inverse problem, which is solved based on the forward problem: predict the EL given

the parameters. By solving the inverse problem, we provide a more guided approach to design tunable elements for multistable structures.

The rest of this article is organized as follows. In Section II, we discuss how to tune the EL of a beam-based module by adjusting the parameters of its components. In Section III, we implement the tuning strategies on prototypes to realize different ELs. We also address the forward problem by establishing a model to predict the EL and conducting experiments to validate the developed model. In Section IV, we address the inverse problem to solve for the correct tuning parameters which result in the desired EL for the tunable module. In Section V, we demonstrate the wide applicability of this tunable module with a kicker, a reconfigurable arm, and a crawling robot. Finally, Section VI concludes this article.

## II. WORKING PRINCIPLE FOR TUNING THE ELs

In this section, we explain how to actively tune the ELs of modules with elastic instabilities. Without loss of generality, we use a beam-based module with a linear spring to illustrate the working principle. This module primarily comprises a flexible beam and an elastomeric spring [see labels on the right of Fig. 1(a)]. The beam is connected to two rigid frames (top and bottom). One end of the spring is anchored to the top frame at point P, while the other end is connected to an adjustable cable, which is, in turn, attached to the bottom frame at point Q. The adjustable cable of length  $L_c$  is used to offset the extension of the spring. When the dimension and bending angle of the flexible beam are given, increasing the length of the adjustable cable results in a decrease in the length or extension of the spring. The beam has a rectangular hole at its center, allowing for the passage of both the spring and the adjustable cable as the beam undergoes bending motions. With an initially straight flexible beam, this module exhibits two symmetrical stable states (SS): The left stable state (left SS) and the right stable state (right SS), each mirroring the other relative to the beam's straight configuration [Fig. 1(a)].

To analyze the stable states, we need to consider the module's strain energy. The total strain energy ( $U$ ) of the module consists of two components: 1) the strain energy of the flexible beam ( $U_b$ ); and 2) the spring ( $U_s$ ). Since the flexible beam is long and slender, the strain energy of the bent beam due to shear stress and compressive stress is negligible compared with that due to normal stress. So  $U_b$  mainly comes from the bending energy of the flexible beam, while  $U_s$  comes from the spring's extension. We can represent the total energy  $U$  as a function of the beam's bending angle  $\theta$

$$U = U_b + U_s = \frac{1}{2}k_b(\theta - \theta_{in})^2 + \frac{1}{2}k_s\Delta^2(\theta) \quad (1)$$

where  $k_b$  is the beam's effective bending stiffness,  $\theta_{in}$  is the beam's initial bending angle ( $\theta_{in} = 0$  for an initially straight beam), and  $k_s$  is the spring's stiffness.  $\Delta(\theta)$  represents the spring's extension as a function of  $\theta$ , which can be expressed as

$$\Delta(\theta) = \max(0, L(\theta) - L_c - L_{in}) \quad (2)$$

where  $L(\theta)$ , varying with  $\theta$ , is the distance between the two anchoring points P and Q,  $L_c$  is the length of the adjustable cable,  $L_{in}$  is the spring's nominal length. As can be seen in (2),  $L_c$  can be used to offset the extension of the spring for a given  $L(\theta)$ . Assuming the beam is uniformly deformed and takes on the shape of a circular arc,  $L(\theta)$  is a chord PQ corresponding to this circular arc. The radius of the arc is expressed as  $R(\theta) = L_t/\theta$ , where  $L_t$  is the length of the beam. In this case,  $L$  can be obtained as a function of  $\theta$  by the following equation:

$$L(\theta) = 2R \sin\left(\frac{\theta}{2}\right) = 2\frac{L_t}{\theta} \sin\left(\frac{\theta}{2}\right). \quad (3)$$

With (1), we plot  $U$ ,  $U_b$ , and  $U_s$  as functions of the bending angle  $\theta$ , represented by the black, red, and green curves, respectively [Fig. 1(b)]. The beam's strain energy,  $U_b$ , is a convex parabola with its vertex located at  $(\theta_{in}, 0)$ . The spring's strain energy,  $U_s$ , is symmetric about the vertical axis  $\theta = 0$ . The resulting total EL of the module,  $U = U_b + U_s$ , has two local minima at  $\theta_l$  and  $\theta_r$  [shown as the black squares in Fig. 1(b)], indicating the left and right stable states (left SS and right SS) of the module. The module is in equilibrium when the bending angle  $\theta$  equals  $\theta_l$  or  $\theta_r$ , and external energy is required to shift the module away from the stable states ( $\theta_l$  or  $\theta_r$ ). The peak of this EL [ $U_p$ , shown as the black dot in Fig. 1(b)], indicating the module's maximal strain energy and its unstable straight state, is located at  $\theta = 0$ . The differences between the energy peak ( $U_p$ ) and energies at the local minima ( $U_l$  or  $U_r$ ) are termed the energy barriers (i.e., left energy barrier  $E_{bar}^l = U_p - U_l$  and right energy barrier  $E_{bar}^r = U_p - U_r$ ). We call this configuration SB since the EL is bistable with two minima ( $\theta_l$  and  $\theta_r$ ) and symmetric ( $\theta_r = -\theta_l$ ).

To transit the module from the right SS to the left SS, we apply a force to bend the module to the left, overcoming the right energy barrier  $E_{bar}^r$ . Application of this external force will increase the strain energy stored in the module. Once the module surpasses the energy peak  $U_p$ , part of the stored strain energy would be instantly released, resulting in a rapid snap motion to the left SS. A similar mechanism is needed when switching from the left to the right SS, where an appropriate force must overcome the left energy barrier  $E_{bar}^l$  to initiate the transition.

By tuning the EL, we can adjust the positions of the two resting angles ( $\theta_l$  and  $\theta_r$ ). If the magnitudes of  $\theta_l$  and  $\theta_r$  are adjusted to be different ( $|\theta_r| \neq |\theta_l|$ ), the module is referred to as AB. If one resting angle disappears, the module will become monostable (MS). Similarly, the value of each energy barrier ( $E_{bar}^l$  and  $E_{bar}^r$ ) can also be adjusted by tuning the EL. An increase in  $E_{bar}^r$ , for instance, leads to a more rapid or forceful transition from the left to the right SS [solid curved arrow in Fig. 1(b)] since a greater amount of stored energy is released upon surpassing the energy peak  $U_p$ . Meanwhile, this increase in  $E_{bar}^r$  makes it more difficult to transit from the right to the left SS since more energy input is required to overcome a larger  $E_{bar}^r$ .

Since we have four independent tunable elements:  $k_b$ ,  $\theta_{in}$ ,  $k_s$ , and  $L_c$  in (1) and (2), in theory, we can simultaneously achieve all the four desired characteristics ( $\theta_l$ ,  $\theta_r$ ,  $E_{bar}^l$ , and  $E_{bar}^r$ ) by choosing proper values for  $k_b$ ,  $\theta_{in}$ ,  $k_s$ , and  $L_c$ . In practice, however, it is quite challenging to concurrently tune these four

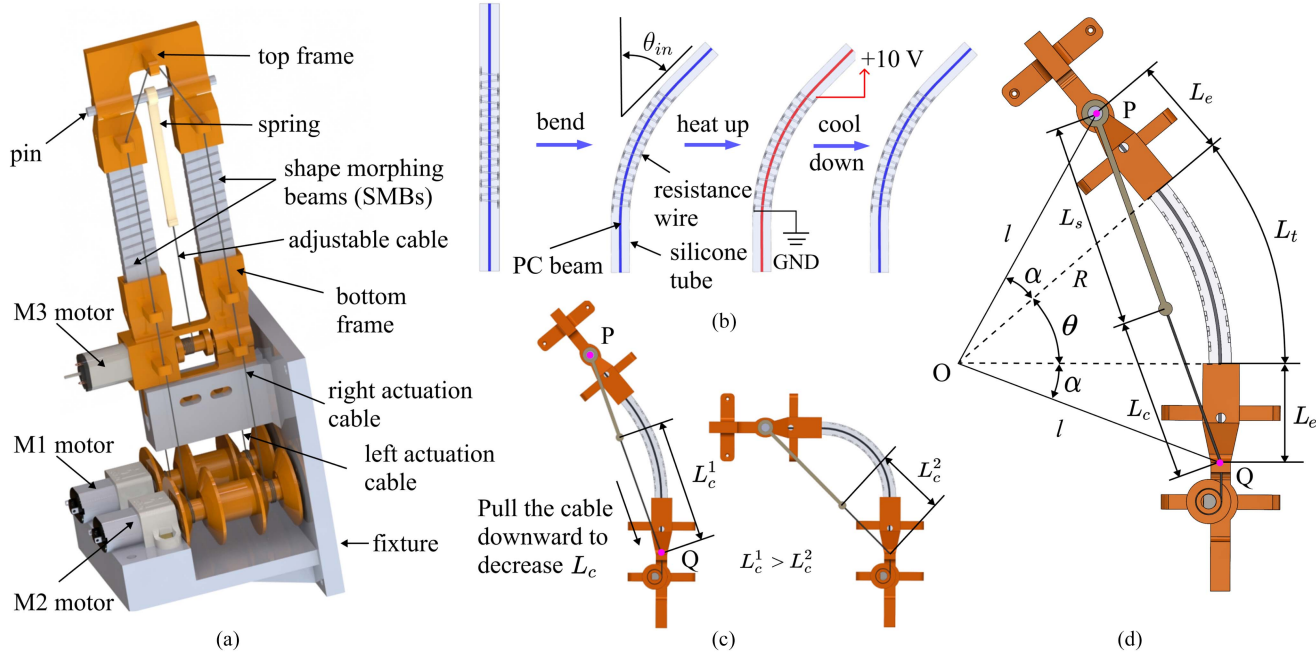


**Fig. 2.** Implementation of the two tuning strategies and the forward modeling. (a) 3D model of the tunable module in its straight shape with key components: The SMBs, the spring, and three dc motors (M1, M2, and M3). (b) The structure of the SMBs and the procedure to tune their initial bending angle  $\theta_{in}$ . (c) The procedure to tune the cable's length  $L_c$ . (d) Geometric parameters of the module for developing a more accurate forward model.

tunable elements in a tunable module. In addition, it is generally not necessary to achieve all four characteristics at the same time (e.g., in some cases, only the resting angles are required, and the energy barriers are not critical). Therefore, in this study, we only investigate strategies to adjust two elements on the fly,  $\theta_{in}$  and  $L_c$ , to tune the EL to achieve either two desired resting angles (indicating the stable states of the module) or two desired energy barriers (indicating the dynamic responses of the module). We choose to adjust  $\theta_{in}$  and  $L_c$  because they are relatively easy to implement and prove effective in achieving the desired characteristics (implementation details are discussed in Section III).

We first illustrate how adjusting the beam's initial bending angle ( $\theta_{in}$ ) can influence the module's EL. Since  $U_b = \frac{1}{2}k_b(\theta - \theta_{in})^2$ , adjusting  $\theta_{in}$  will influence the energy profile of the flexible beam. Specifically, adjusting  $\theta_{in}$  can shift  $U_b$  horizontally since  $U_b$  is a convex parabola symmetric about vertical axis  $\theta = \theta_{in}$ . To illustrate this, we plot the module's ELs [Fig. 1(c)] for three different  $\theta_{in}$  values:  $0^\circ$ ,  $40^\circ$ , and  $80^\circ$ , while maintaining a constant  $L_c$  at 17 mm. For these three cases, the energy profile of the spring,  $U_s$ , stays the same. However,  $U_b$  will shift horizontally to the right when  $\theta_{in}$  increases, thus changing the module's EL,  $U$ . When  $\theta_{in} = 0^\circ$ , the module's EL is SB. When  $\theta_{in} = 40^\circ$ , the EL changes to AB. Values of energy barriers are also changed. Compared with the first case ( $\theta_{in} = 0^\circ$ ),  $E_{bar}^l$  decreases while  $E_{bar}^r$  increases. When  $\theta_{in} = 80^\circ$ , the peak disappears, eliminating the energy barriers and resulting in an MS configuration.

We then illustrate how adjusting the cable's length ( $L_c$ ) will influence the module's EL. Since  $\Delta(\theta) = \max(0, L(\theta) -$

$L_c - L_{in})$  and  $U_s = \frac{1}{2}k_s\Delta^2(\theta)$ , adjusting  $L_c$  will influence the extension of the spring, thereby affecting the energy profile of the elastic spring. Specifically, changing  $L_c$  will scale up or down the energy profile of the spring. We plot the module's ELs [Fig. 1(d)] for three different  $L_c$  values: 10, 15, and 20 mm, while maintaining a constant  $\theta_{in}$  at  $0^\circ$ . For these three cases,  $U_b$  stays the same, but  $U_s$  will scale down when we increase  $L_c$ , thus changing the module's EL,  $U$ . The module is SB for each case since both  $U_s$  and  $U_b$  are symmetric about the vertical axis ( $\theta = 0^\circ$ ). In these three cases, the module with  $L_c = 10$  mm has the largest energy barriers ( $E_{bar}^l$  and  $E_{bar}^r$ ). When  $L_c$  increases, the resting angles move closer to  $0^\circ$ , until the energy peak of the EL (shown as the black dot) finally disappears, and the module becomes monostable.

### III. IMPLEMENTATIONS OF THE TWO TUNING STRATEGIES

In this section, we detail how we implement the tunable module and the two tuning strategies for the beam's initial bending angle  $\theta_{in}$  and the cable's length ( $L_c$ ). We also develop a more accurate forward model to predict the module's EL to realize three different configurations (SB, AB, and MS) by adjusting  $\theta_{in}$  and  $L_c$  on the fly.

#### A. Design of the Tunable Module

The developed module is made of several parts. We use a straight configuration of the module in Fig. 2(a) for a better illustration. First, it has two SMBs that can morph to and then hold another curved shape, thereby adjusting their initial bending angles (details in the next paragraph). One end of these SMBs

is connected to a 3-D printed top frame, and the other to a 3-D printed bottom frame, which is mounted to a fixture. An elastic spring made from elastomers (details to be discussed later) is placed in the middle of the two SMBs. One end of the spring is attached to a pin on the top frame, while the other end is attached to an adjustable cable that can be pulled or released by a dc motor M3 (3080, Pololu Corp) placed in the bottom frame. The fixture hosts two additional dc motors labeled as M1 and M2 (3080, Pololu Corp) placed on each side of the module. Actuating M1 will pull the left actuation cable to bend the module to the left, provided that the right actuation cable is slack. Similarly, actuating M2 can pull the right actuation cable to bend the module to the right. The bending angle is negative (positive) if it is bent to the left (right) by the left (right) actuation cable. The attainable range of the bending angle  $\theta$  is  $(-192^\circ, 192^\circ)$ , which is determined by the collision of the two frames. In practice, we only bend the module in the range  $(-160^\circ, 160^\circ)$ , to reduce the influence of permanent plastic deformation of the bending beam. On both the top and bottom frames, several protrusions with holes are designed to facilitate the routing of the actuation cables.

Tuning  $\theta_{in}$  is accomplished through the SMBs [Fig. 2(b)]. Each SMB has three components: A 3-D printed beam made from thermoplastic material polycarbonate (PC), a customized silicone tube encasing the beam, and a resistance wire wrapped around the tube. The beam is initially straight [i.e.,  $\theta_{in} = 0^\circ$ , Fig. 2(a)]. Now we can actuate either M1 or M2 to bend the SMBs to a desired angle  $\theta_{in}$  to the left or right. Then, we heat up the tubes and the PC beams by applying a constant voltage (10 V) across the resistance wires [Fig. 2(b)]. The silicone tubes serve a dual purpose: 1) they facilitate uniform heating of the PC beams; and 2) ensure consistent bending behavior during the bending motion. After around 200 s, the PC beams reach a temperature higher than their glass transition temperature and become soft. Then, we maintain the new shape for around 320 s while cooling down the SMBs until their temperature drops below the glass transition temperature, and the SMBs regain their rigidity. Finally, we release the actuation cables. During this tuning process, we keep the spring slack because, with tension in the spring, the heated beams may buckle due to the restoring force of the spring. In this way, we can actively adjust the initial bending angle of the module on the fly.

Tuning the length of the adjustable cable,  $L_c$ , is realized by using the cable system driven by motor M3. One end of the cable is attached to the lower end of the spring, while the other end is attached to a capstan on the shaft of M3. The cable is routed through a small hole in the bottom frame [see point Q in Fig. 2(c) and 2(d)] to keep the effective length of the cable  $L_C$  constant when the module undergoes bending motion. In this way, we can actuate M3 to adjust the value of  $L_c$  [Fig. 2(c)]. M3 is also used to relax the spring before tuning the initial bending angle of the SMBs.

We choose polycarbonate (PolyMax PC, Polymaker Inc) for the beams since it can maintain its initial shape better, i.e., it can almost recover its initial shape after being bent by a large angle and undergoing a large strain, compared with other 3-D printing materials (e.g., PLA, PETG, and Nylon). We design the

dimension of the beam to be  $0.6 \times 8 \times 38$  mm, and fabricate the beam through 3-D printing (Prusa i3 MK3). The customized silicone tube is molded using Dragon Skin 30 (Smooth-On Inc) with an outside dimension of  $4.5 \times 11 \times 38$  mm. A dedicated mold for curing the silicone tube is printed with a FDM printer (Prusa i3 MK3). A beam with the same dimension as those used in the SMBs is inserted to the center of the mold to realize the rectangular hole in the cured silicone tube. After inserting the PC beam to the cured silicone tube, a resistance wire (RW0332, TEMCo Inc) with a resistance of  $9 \Omega$  is wrapped outside the tube to complete the fabrication of an SMB. The elastic spring is also molded using Dragon Skin 30 because it can withstand a large tensile strain. We choose the spring's dimension to be  $4 \times 2.4 \times 32$  mm. We select the specific dimensions for the beam and the spring such that their strain energies during the bending process are approximately within the same range.

### B. Forward Problem: Predict the Tunable Module's EL

With the detailed design, we now establish a more accurate mathematical model for the EL to investigate how tunable elements  $\theta_{in}$  and  $L_c$  will influence the module's EL (i.e., resting angles or energy barriers). Specifically, we want to solve the forward problem: given the values for  $\theta_{in}$  and  $L_c$ , predict the module's EL.

In the implemented module, the total strain energy has three parts: 1) the strain energies from the tubes  $U_t$ ; 2) the beams  $U_b$ ; and 3) the spring  $U_s$ .

$$U(\theta) = U_t + U_b + U_s$$

$$= 2 \times \frac{1}{2} k_t \theta^2 + 2 \times \frac{1}{2} k_b (\theta - \theta_{in})^2 + \frac{1}{2} k_s \Delta^2(\theta) \quad (4)$$

where  $k_t$  is the effective bending stiffness of the two tubes, and other parameters are the same as in (1). Note that  $U_t = \frac{1}{2} k_t \theta^2$  because the initial angle of both tubes is always zero, regardless of the value of  $\theta_{in}$ . Now, since there exists a distance [ $L_e$  in Fig. 2(d)] between the end of the bending beam and the spring's attaching point (P or Q), (3) does not hold anymore. Based on the geometry shown in Fig. 2(d), we have the following equation to relate  $L$  and  $\theta$ :

$$L(\theta) = \begin{cases} 2l \sin\left(\frac{|\theta|}{2} + \alpha\right), & \text{if } \theta \in (-\pi, 0) \cup (0, \pi) \\ 2L_e + L_t, & \text{if } \theta = 0 \end{cases} \quad (5)$$

where  $l = \sqrt{L_e^2 + L_t^2/\theta^2}$ ,  $L_t$  is the length of the tube,  $\alpha = \arctan(|\theta|L_e/L_t)$ . Equations (4) and (5) can be used to predict the EL of a tunable module given the values of the two tuning parameters  $\theta_{in}$  and  $L_c$ .

We can obtain the derivative of  $L(\theta)$  with respect to  $\theta$  as

$$\begin{aligned} L'(\theta) = & \left[ -\frac{2L_t^2}{l|\theta|^3} \sin\left(\frac{|\theta|}{2} + \alpha\right) \right. \\ & \left. + l \cos\left(\frac{|\theta|}{2} + \alpha\right) \left( 1 + \frac{2L_e L_t}{\theta^2 l^2} \right) \right] \frac{|\theta|}{\theta} \end{aligned} \quad (6)$$

for the special case of  $\theta = 0$ ,  $L'(\theta) = 0$ .

The configuration of the module (i.e., SB, AB, or MS) can be determined by examining the derivative of  $U$  with respect to  $\theta$ .

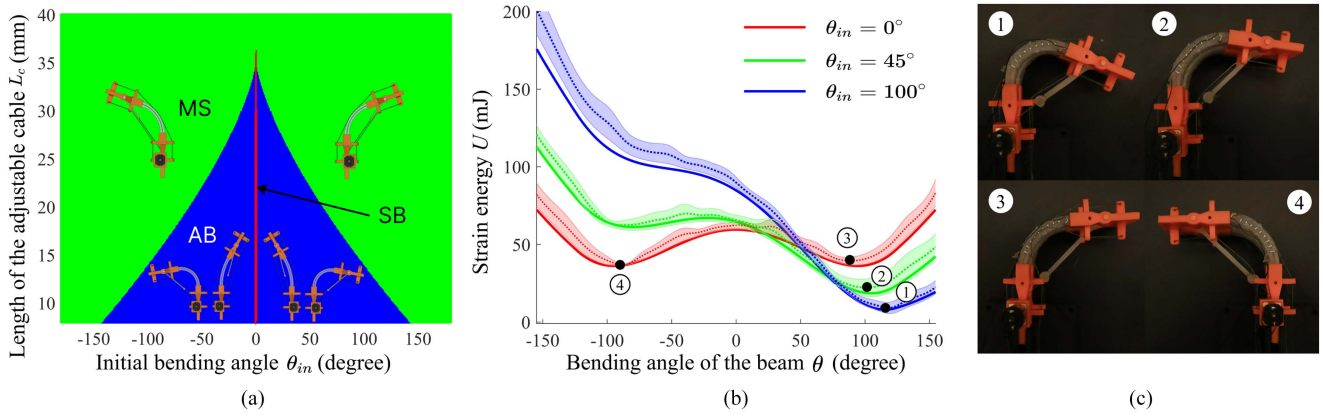


**Fig. 3.** Validation of the forward model. (a) Configurations of the module (SB, AB, and MS) depend on the two adjustable elements ( $\theta_{in}$  and  $L_c$ ). (b) Comparisons between the measured and predicted ELs of the tunable module in three different configurations. (c) Selected pictures of the tunable module in its stable states.

Specifically, if the equation

$$U'(\theta) = 0 \quad (7)$$

has three solutions  $\theta_1$ ,  $\theta_2$ , and  $\theta_3$ ,  $U(\theta)$  would have three extrema (one maximum point at  $\theta_2$  and two minimum point at  $\theta_1$  and  $\theta_3$ ), indicating the module is bistable. The maximum and minima represent the energy peak and stable states, respectively, as shown by the black dots and squares in Fig. 1(b)–(d). Further, the module is SB or AB if the magnitudes of the two minima are the same or different. If (7) has one solution, then  $U(\theta)$  has one minimum, indicating the module is MS. If (7) has two solutions,  $U(\theta)$  is transitioning between bistable and monostable (the maximum point  $\theta_2$  and one minimum  $\theta_1$  or  $\theta_3$  are merged).

Carrying out the derivative, we have

$$U'(\theta) = 2k_t\theta + 2k_b(\theta - \theta_{in}) + k_s\Delta(\theta)L'(\theta) \quad (8)$$

where  $\Delta(\theta) = \max(0, L(\theta) - L_c - L_{in})$ .

A MATLAB script is developed to numerically solve (7) using the built-in fmincon function to obtain the bending angles ( $\theta_1$ ,  $\theta_2$ , and  $\theta_3$ ) corresponding to the maximum and minimum points on the energy landscapes [black dots and squares in Fig. 1(b)–(d)]. Based on these obtained bending angles, the energy peak, minimum energies at stable states, and energy barriers can be calculated using (4). In this way, the forward model can be used to both predict the EL of a module and solve for its resting angles and energy barriers.

To gain insights on how  $\theta_{in}$  and  $L_c$  will influence the module's behavior, we use (7) to plot the bistable and monostable regions in Fig. 3(a). For this analysis, we experimentally obtain the values of parameters  $k_t = 1.620$  mJ,  $k_b = 8.296$  mJ, and  $k_s = 0.1518$  mJ/mm<sup>2</sup> (detailed procedures can be found in the supplementary material). We have also limited the range of  $\theta_{in}$  to  $(-\pi, \pi)$  and  $L_c$  to  $(8, 40)$ . We choose this range for  $L_c$  because if  $L_c$  is too small, the spring force of the module around its straight shape would be very large, leading to the buckling of the beam during the transition. A thorough discussion on the buckling behavior of flexible beams could be found in [31]. If  $L_c$  is too large (e.g., 48 mm), then the spring will always be slack, and the module is always monostable.

In Fig. 3(a), we see that all the regions are symmetric about the axis  $\theta_{in} = 0$ . The SB configuration is only possible when  $\theta_{in} = 0$  and  $L_c < 36.1$  mm. When  $\theta_{in} = 0$  and  $36.1 < L_c < 40$  mm [the spring's energy will decrease if  $L_c$  increases, see Fig. 1(d)], the spring's energy profile is insufficient to result in a maximum in the module's EL. So, the module is also monostable. For a given value of  $L_c < 36.1$  mm, the module will go from bistable to monostable when the magnitude of  $\theta_{in}$  increases, as indicated by Fig. 1(c). At the boundary between bistability and monostability (i.e., the transition between bistable and monostable ELs), (7) has two solutions. The magnitude of  $\theta_{in}$  at this boundary increases when  $L_c$  decreases. This is because, as shown in Fig. 1(c), if the green curve is higher (corresponding to lower  $L_c$ ), the red curve needs to shift more (corresponding to larger  $\theta_{in}$ ) horizontally to transition the module's EL from bistable to monostable. Based on the results in Fig. 3(a), we can choose specific values for  $\theta_{in}$  and  $L_c$  of the prototype to enable three different configurations of the EL: SB, AB, and MS.

To validate the model we have developed so that we can use it for the inverse problem in the next section, we experimentally obtain the ELs of modules with different configurations (SB, AB, and MS) and compare them with the predicted ELs. We conducted experiments on the same module with different  $\theta_{in}$  and the same  $L_c = 20$  mm. These correspond to three different configurations: SB, AB, and MS, respectively. Since it is difficult to directly measure the strain energy, we derive the strain energy through bending tests of the module (detailed experimental procedures for these tests can be found in the supplementary material) to obtain the force on the actuation cable and displacement of the actuation cable. Then, we calculate the strain energy through discrete integration of the force on the cable over displacement of the cable. For this discrete integration, we choose the initial condition (i.e., the initial energy) as the strain energy at the left stable state (or the right stable state for a monostable module) which can be calculated using (4).

For each module, the bending test is repeated three times to obtain three ELs. Both experimental and predicted ELs are

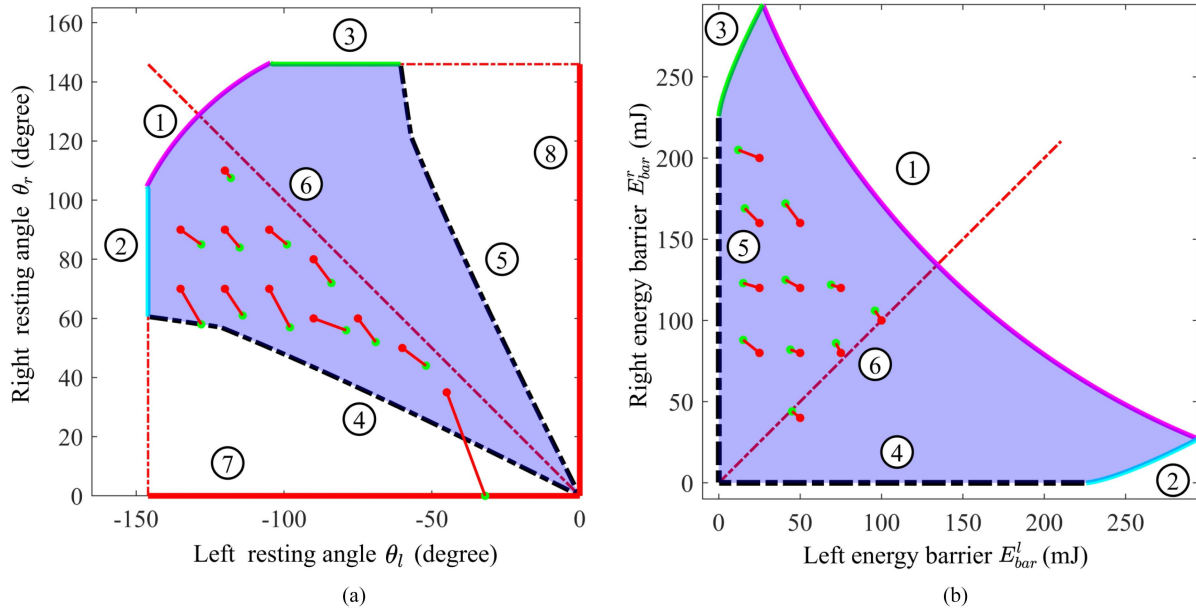


**Fig. 4.** Feasible regions of resting angles or energy barriers when  $-\pi < \theta_{in} < \pi$ ,  $8 < L_c < 40$ . (a) Feasible region of resting angles ( $\theta_l$  and  $\theta_r$ ). (b) Feasible region of energy barriers ( $E_{\text{bar}}^l$  and  $E_{\text{bar}}^r$ ).

plotted in Fig. 3(b), where the dotted and solid curves are the experimental and predicted ELs, respectively. Shaded regions around the dotted curves show the standard deviations of the measurements. From this figure, we can see that the strain energy model matches reasonably well with the experimental results with an average error of 6.61 mJ and average standard deviation of 8.87 mJ. The experimental energies are greater than the predicted ones, possibly because of the friction force between the actuation cables and the silicone tubes. Four images representing typical stable states of the tunable module are illustrated in Fig. 3(c).

#### IV. INVERSE PROBLEM: OBTAIN DESIRED EL USING THE TWO TUNING STRATEGIES

Using the two tuning strategies, a more interesting problem is to achieve a desired EL. Though the most general case is to achieve precisely the same desired EL (i.e., the exact curve of the EL) for a tunable module, the most important characteristics for the EL are the resting angles ( $\theta_l$ ,  $\theta_r$ ) and the energy barriers ( $E_{\text{bar}}^l$ , and  $E_{\text{bar}}^r$ ). Ideally, we can achieve both the desired resting angles and desired energy barriers at the same time by tuning the four elements ( $k_b$ ,  $\theta_{in}$ ,  $k_s$ , and  $L_c$ ) concurrently. However, we only implemented two independent strategies to adjust  $\theta_{in}$  and  $L_c$  on the fly as discussed in Section III. Therefore, in this section, we aim to solve the simplified tuning problem: given desired resting angles ( $\theta_l$  and  $\theta_r$ ) or energy barriers ( $E_{\text{bar}}^l$  and  $E_{\text{bar}}^r$ ), solve for the values of  $\theta_{in}$  and  $L_c$ . We call this the inverse problem for tuning as opposed to the forward problem discussed in Section III-B. We also validate the solution by implementing the two tuning strategies on a prototype and comparing the resulting resting angles (or energy barriers) with the desired ones.

##### A. Feasible Regions of the Resting Angles or Energy Barriers

Before trying to realize the desired resting angles or energy barriers, it is necessary to first obtain the feasible regions for them so that we can choose the desired values in these regions. We first discuss the feasible region for the resting angles, which can be categorized into two cases: 1) when the module is bistable, find the region for two variables  $\theta_l$  and  $\theta_r$ , whereas; 2) when the module is monostable, only the region for one variable needs to be determined.

When the module is bistable, the feasible region of resting angles  $\theta_l$  and  $\theta_r$  depends on two conditions: 1) ranges of the tunable parameters ( $\theta_{in}$  and  $L_c$ ); and 2) bistability of the module. We look at these two conditions to determine the values for  $\theta_{in}$  and  $L_c$  corresponding to the boundaries of the feasible region. Using the forward model developed in Section III-B, we can obtain  $\theta_l$  and  $\theta_r$  resulting from those tuning parameters  $\theta_{in}$  and  $L_c$ . Then,  $\theta_l$  and  $\theta_r$  are plotted in a 2-D figure to show the boundaries of the feasible region.

For the first condition, we can generate three boundaries: ①, ②, and ③ in Fig. 4(a) based on the ranges of tunable parameters.

$$\text{curve ① : } L_c = 8, -\pi < \theta_{in} < \pi \quad (9)$$

$$\text{curve ② : } \theta_{in} = -\pi, 8 < L_c < 40 \quad (10)$$

$$\text{curve ③ : } \theta_{in} = \pi, 8 < L_c < 40. \quad (11)$$

For instance, for the range described by (9), we take sample sets (e.g.,  $\theta_{in} = \pi/4$  and  $L_c = 8$  mm) from this range and use (7) to determine if the module for a certain sample set of  $\theta_{in}$  and  $L_c$  is bistable or not. If bistable, we record the corresponding  $\theta_l$  and  $\theta_r$  for that sample set using the forward model. Plotting the resting angles for all the sample sets, we obtain boundary ①. The ranges

described by (10) and (11) are utilized in a similar manner to get boundaries ② and ③. When  $L_c = 40$ , the module is always monostable, so this upper bound of  $L_c$  is irrelevant in Fig. 4(a). For the second condition, we can generate two boundaries ④ and ⑤ in Fig. 4(a), corresponding to the transition of the module from bistability to monostability, which occurs when (7) has just two solutions (see the supplementary material for the detailed procedure to obtain boundaries ④ and ⑤). These two sets of boundaries form a closed region [the blue region in Fig. 4(a)], inside which the input variables  $\theta_{in} \in (-\pi, \pi)$  and  $L_c \in (8, 40)$  and the module will be bistable. In other words, we can realize any values for  $\theta_l$  and  $\theta_r$  inside this region by choosing proper values of  $\theta_{in}$  and  $L_c$ . Curve ⑥ is plotted here to show the SB configurations.

When the module is monostable, we can only obtain the region for one resting angle. In this case, we use  $\theta_l$  (or  $\theta_r$ ) to designate the resting angle of the module if it is negative (or nonnegative). Curves ⑦ (representing  $\theta_l$ ) and ⑧ (representing  $\theta_r$ ) are also determined by the two conditions mentioned above. It can be seen that the region of  $\theta_l$  (or  $\theta_r$ ) extends from 0 to the resting angle resulting from tunable parameters  $\theta_{in} = -\pi$  (or  $\pi$ ) and  $L_c$ , when the module transitions from bistable to monostable.

We then try to get the feasible region for the energy barriers  $E_{bar}^l$  and  $E_{bar}^r$ . When the module is bistable, similar to the case of resting angles, the feasible region of  $E_{bar}^l$  and  $E_{bar}^r$  also depends on two conditions: 1) ranges of the tunable parameters ( $\theta_{in}$  and  $L_c$ ); and 2) bistability of the module. As shown in Fig. 4(b), the feasible region of  $E_{bar}^l$  and  $E_{bar}^r$  is enclosed by two sets of boundaries: 1) (①, ②, and ③) determined by the ranges of the tunable parameters ( $\theta_{in}$  and  $L_c$ ); and 2) (④ and ⑤) determined by the transition of the module between bistable and monostable states. Curve ⑥ is also plotted here to show the SB configurations. Note that for monostable configurations, the energy barrier does not exist. In addition, boundaries ④ and ⑤ in Fig. 4(b) lie on the horizontal and vertical axes, respectively, since one energy barrier is 0 when the module transitions between bistable and monostable states.

### B. Obtain Desired Resting Angles or Energy Barriers

After identifying the feasible regions for the resting angles and energy barriers, we can solve the inverse problem: given desired resting angles ( $\bar{\theta}_l$  and  $\bar{\theta}_r$ ) or energy barriers ( $\bar{E}_{bar}^l$  and  $\bar{E}_{bar}^r$ ) from the closed regions shown in Fig. 4, solve for the corresponding tuning parameters  $\theta_{in}$  and  $L_c$ .

First, we investigate the inverse problem for tuning the resting angles. When a module is at a resting angle, the derivative of its strain energy with respect to the bending angle is 0. So the desired resting angles  $\bar{\theta}_l$  and  $\bar{\theta}_r$  must both satisfy (7), leading to the following two equations with  $\theta_{in}$  and  $L_c$  being the unknowns:

$$(k_s + k_b)\bar{\theta}_l - k_b\theta_{in} + k_s \max(0, L(\bar{\theta}_l) - L_c - L_{in})L'(\bar{\theta}_l) = 0 \quad (12)$$

$$(k_s + k_b)\bar{\theta}_r - k_b\theta_{in} + k_s \max(0, L(\bar{\theta}_r) - L_c - L_{in})L'(\bar{\theta}_r) = 0. \quad (13)$$

Equations (12) and (13) can be solved to determine the values of the tuning parameters  $\theta_{in}$  and  $L_c$ . In this case, if we tune the

module to have the solved  $\theta_{in}$  and  $L_c$ , ideally, the resting angles of the resulting module should be  $\bar{\theta}_l$  and  $\bar{\theta}_r$ .

To validate the inverse solution obtained thorough (12) and (13), we choose 12 sets of specific values for  $\bar{\theta}_l$  and  $\bar{\theta}_r$  in the closed region in Fig. 4 (detailed values are provided in the supplementary material). Since the closed region is symmetric about curve ⑥, we just choose points on one side of the curve. For each set (shown as red dots in Fig. 4), we plug in values of  $\bar{\theta}_l$  and  $\bar{\theta}_r$  to (12) and (13) to solve for the corresponding tuning parameters  $\theta_{in}$  and  $L_c$  and then implement them on the prototype using the two tuning strategies. Finally, we measure the resulting resting angles and compare them with the desired ones  $\bar{\theta}_l$  and  $\bar{\theta}_r$ . The results are shown in Fig. 4, where the red and green dots represent the desired and the measured resting angles, respectively. For each set, a red line is used to connect the measured to the desired value. It can be seen that they match well with a mean error of  $8.2^\circ$  and a standard deviation of  $3.5^\circ$ . The error may be caused by the viscoelastic behavior and plastic deformation of the bending beams, as well as the deformation of the silicone tubes under high temperatures. For the case with  $\bar{\theta}_l = -45^\circ$  and  $\bar{\theta}_r = 35^\circ$ , the resulted prototype becomes monostable after tuning, instead of bistable as expected. We believe this is because the imperfect behaviors of the bending beams and tubes overwhelm the small energy barrier of the prototype.

For the monostable case, we have only one resting angle ( $\bar{\theta}_l$  or  $\bar{\theta}_r$ ) and one valid constraint equation ( (12) or (13)) to solve for  $\theta_{in}$  and  $L_c$ . With only one equation, we can still realize the given resting angle  $\bar{\theta}_l$  (or  $\bar{\theta}_r$ ) by first choosing a specific value for  $L_c$  and then solving for  $\theta_{in}$  using (12) (or (13)) based on the chosen  $L_c$ .

For the inverse problem for tuning the energy barriers, there are no simple linear equations similar to (12) and (13). Instead, simplex search optimization method is used to solve for the values of the tuning parameters  $\theta_{in}$  and  $L_c$  given the desired energy barriers  $\bar{E}_{bar}^l$  and  $\bar{E}_{bar}^r$ . The objective function used in the optimization is the error between the desired energy barriers and that resulting from the tuning parameters  $\theta_{in}$  and  $L_c$ . We also conduct experiments to validate the inverse solution for energy barriers obtained through the optimization method. We also choose 12 sets of specific values for  $\bar{E}_{bar}^l$  and  $\bar{E}_{bar}^r$  in the closed region in Fig. 4(b). Following a procedure similar to that for the resting angles, we implement the two tuning strategies on a prototype and compare the desired and measured energy barriers. Red and green dots represent the desired and measured energy barriers, respectively. As shown in Fig. 4(b), they match well with a mean error of 9.7 mJ and a standard deviation of 4.5 mJ. It can be seen that for each set, the measured values are predominantly situated to the upper left of the desired values. This may be attributed to the permanent deformation of the silicone tubes caused by high temperatures when implementing the tuning strategies.

## V. APPLICATIONS

In this section, we employ the tunable modules for three different applications to demonstrate the utility of tuning EL on the fly.

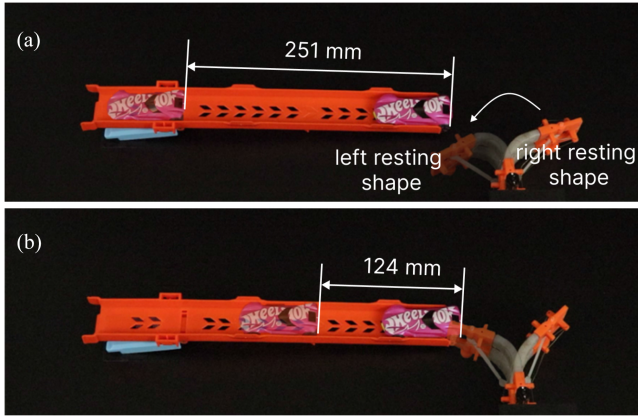


**Fig. 5.** Kicker based on a single tunable module has adjustable kicking power. (a) When  $\theta_{in} = -\pi/4$  and  $L_c = 10$  mm, the toy car travels by 251 mm. (b) When  $\theta_{in} = -\pi/8$  and  $L_c = 18$  mm, the car travels by 124 mm.

### A. Adjustable Kicker With a Single Tunable Module

We first demonstrate a single tunable module as a kicker that can change its kicking power by adjusting its energy barrier. The tunable module's bottom frame is fixed, while its top frame kicks a toy car on its trajectory during its transition motion. It is initially in its right resting shape. The toy car is placed inside a sloped track to constrain its motion. As shown in the supplementary video and Fig. 5(a), we first let the module have  $\theta_{in} = -\pi/4$  and  $L_c = 10$  mm, which results in a left energy barrier of  $E_{bar}^l = 77.2$  mJ. If we actuate the left cable, the module would first gradually move to the left. Subsequently, upon surpassing the energy peak, it would swiftly release part of its stored strain energy and collide with the toy car during its transition motion. The collision would make the toy car proceed along the sloped track. In this case, the toy car travels a distance of 254 mm. Then, if we want to decrease the traveling distance to approximately half of its current value, we can tune the initial bending angle and the cable length of the tunable module to  $\theta_{in} = -\pi/8$ ,  $L_c = 18$  mm, respectively. This tuning will generate an energy barrier of  $E_{bar}^l = 35.0$  mJ, approximately half of the previous energy barrier. After tuning, we repeat the experiment and find the toy car travels a distance of 124 mm [Fig. 5(b)], also about half of the previous travel distance.

### B. Reconfigurable Arm With Two Tunable Modules

We then connect two modules in series to realize a reconfigurable arm, which can change its resting shapes by employing the two tuning strategies individually. As shown in Fig. 6(a), each module of the arm has its own motor controlling its cable length,  $L_c$ , respectively, but they share the same side motors at the base for actuation. To do this, we route a single cable in a closed loop on each side of the arm. The arm can generate different final shapes by adjusting the resting shapes of both modules independently. Without loss of generality, we show six typical shapes in the arm's workspace.

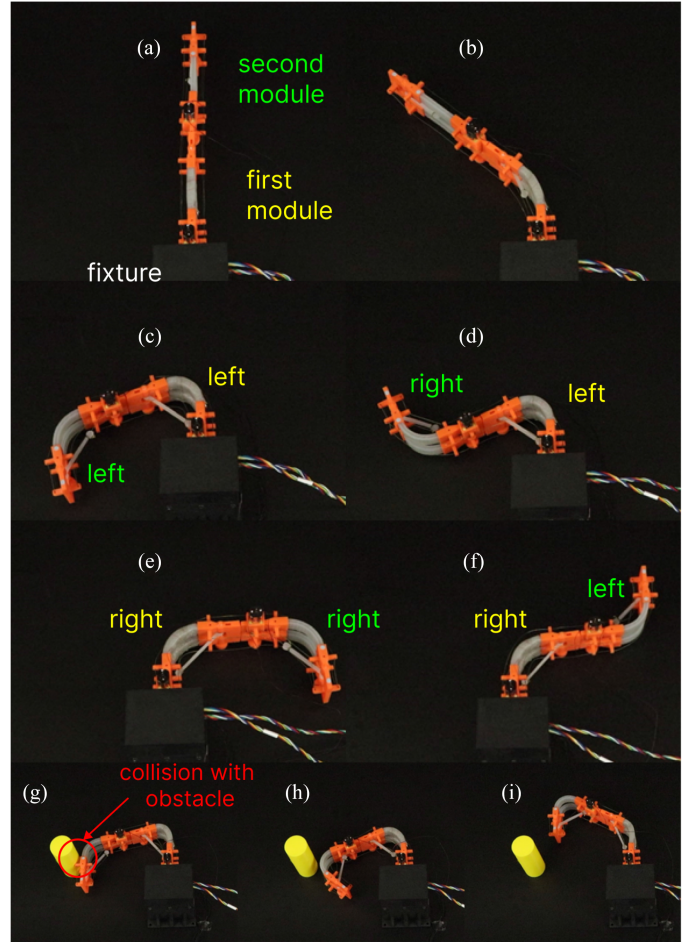


**Fig. 6.** Reconfigurable arm consisting of two modules connected in series can generate different final shapes under the same actuation. Yellow and green texts are for the first and second modules, respectively. The arm is connected to a fixture via the bottom frame of the first module. (a)-(f) are six typical shapes of the arm. (g) Following one route would make the arm collide with an obstacle. (h) and (i) are two sequential images of the arm following another route to avoid colliding with the obstacle.

The first shape is a straight one [Fig. 6(a)], which can be realized by making actuation cables on both sides and adjustable cables on both modules slack. For the second shape, the first module bends left, while the second is straight [Fig. 6(b)]. To generate this shape, we tune the first module to be monostable, with its left resting angle being  $\theta_l^1 = -40^\circ$ . We achieve this resting angle by tuning the first module's initial bending angle to  $\theta_{in}^1 = -62.2^\circ$ . Its adjustable cable is slack.

Shapes C, D, and E share the same initial bending angles and cable lengths for each module. It means the tuning strategies are not required to reconfigure between these three shapes. The first module is AB with  $\theta_l^1 = -120^\circ$  and  $\theta_r^1 = 60^\circ$ , while the second module is SB with  $\theta_l^2 = -90^\circ$  and  $\theta_r^2 = 90^\circ$ . As discussed in Section IV, we can solve for the corresponding values of tuning parameters  $\theta_{in}$  and  $L_c$  for each module via the inverse process of tuning:  $\theta_{in}^1 = -88.4^\circ$ ,  $L_c^1 = 13.4$  mm,  $\theta_{in}^2 = 0^\circ$ ,  $L_c^2 = 21.2$  mm. In shape C [Fig. 6(c)], the second module has a smaller left

energy barrier than the first module. When we actuate the right actuation cable, the second module will transition first (from left to right resting shape) while the first module stays around its left resting shape. In this way, we obtain shape D [Fig. 6(d)]. If we pull the right actuation cable further, the first module will also transition to its right resting shape to generate shape E [Fig. 6(e)]. Under the actuation of the right cable, the reconfigurable arm changes from shape C to E through shape D.

By implementing the tuning strategies, we can also make the first module transition first, thus the arm changes from shape C to shape E through another intermediate shape F [Fig. 6(f)]. To do this, we reduce the value of  $L_c^2$  from 21.2 to 12 mm to increase the left energy barrier of the second module and increase the value of  $L_c^1$  from 13.4 to 21.4 mm to decrease the left energy barrier of the first module. In this way, the first module would transition first when the right actuation cable is pulled, followed by the second module.

Changing the transition sequence (i.e., which module transitions first) can be useful in practical applications. For instance, it can be used to adjust the arm's trajectory to avoid collision with an obstacle (see the supplementary video). As shown in Fig. 6(g), both modules are initially in their left resting shapes. We want to transition the arm to another shape where both modules are in their right resting shapes without colliding with the yellow cylinder obstacle. Following the first route mentioned above (from shape C through D to E) would make the second module collide with the obstacle. Following the latter route (from shape C through F to E) would successfully make the arm finish the transition without colliding with the obstacle. Two intermediate pictures of the arm during this transition are shown in Fig. 6(h) and 6(i).

### C. Reconfigurable Crawling Robot

We further develop a crawling robot to demonstrate that the tuning strategies can be used to change its locomotion direction (see the supplementary video). The robot is made from two modules connected in series, similar to the reconfigurable arm. It has a 3-D printed directional foot on each module [Fig. 7(a)]. The foot on the first and second module is used for the backward and forward locomotion, respectively. To crawl forward, we let the first module maintain its left resting shape while the second module is bent upward by the right actuation cable and downward by the left actuation cable repeatedly [Fig. 7(b)]. We tune the second module with  $\theta_{in}^2 = -30^\circ$  and  $L_c^2 = 25$  mm, which result in energy barriers of  $E_{bar}^l = 22.5$  mJ and  $E_{bar}^r = 0.7$  mJ. We tune the first module with  $\theta_{in}^1 = -90^\circ$  and  $L_c^1 = 15$  mm, which result in a left energy barrier of  $E_{bar}^l = 91.5$  mJ. Both energy barriers of the second module are much smaller than the left energy barrier of the first module. This ensures that when we alternatively actuate the two actuation cables, the first module stays around its left resting shape, while the second module can switch between its two stable states. In this way, the directional foot on the second module can make the robot crawl forward, while the foot on the first module does not touch the ground.

We can change the robot's locomotion direction by tuning the modules' parameters on the fly. To realize the backward crawling [Fig. 7(c)], we first move the foot on the second module away

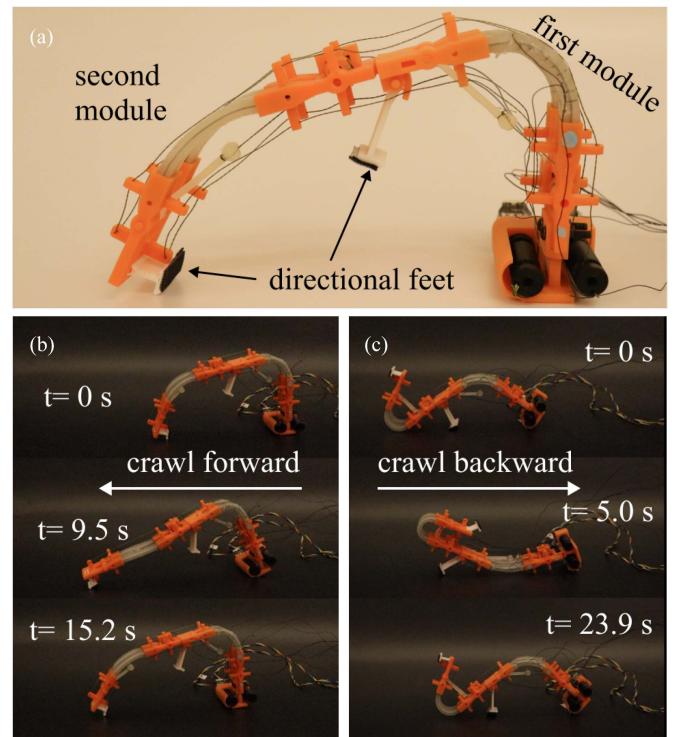


**Fig. 7.** Using the tuning strategy to change the locomotion direction of the crawling robot. (a) To realize the crawling locomotion, two feet capable of directional friction force are attached to the top frame of each module. (b) Some sequential images of the robot crawling forward. (c) Some Sequential images of the robot crawling backward.

from the ground by switching the second module to its right resting shape. Now, the foot on the first module will touch the ground. We then tune the second module with  $\theta_{in}^2 = 90^\circ$  and  $L_c^2 = 8$  mm, resulting in a right energy barrier of 161.2 mJ. We also tune the first module with  $\theta_{in}^1 = -30^\circ$  and  $L_c^1 = 25$ , which results in energy barriers of  $E_{bar}^l = 22.5$  mJ and  $E_{bar}^r = 0.7$  mJ. Both energy barriers of the first module are much smaller than the right energy barrier of the second module. This ensures that when we alternatively actuate the two actuation cables, the second module stays around its right resting shape, while the first module will switch between its two stable states. In this way, the directional foot on the first module would make the robot crawl backward.

## VI. CONCLUSION

In this study, we present methods to tune the EL for a beam-based module with elastic instabilities on the fly without manual alterations. The two tuning strategies we developed—adjusting the beam's initial bending angle and varying the offset of the spring's extension—have proven effective in manipulating the EL, as evidenced by our forward model and its subsequent experimental validation. We have also successfully solved the inverse problem to obtain desired resting angles or energy barriers through the two tuning strategies. We also illustrate the practical applications of tuning through the successful deployment of the tunable module in three different scenarios: 1) as a kicker to impart different energies to an object; 2) as a reconfigurable arm

that can reconfigure its resting shape; and 3) as a crawling robot that can crawl in both directions using the same actuation. Our method may pave the way for future development in advanced robotic and mechatronic systems, leveraging the unique capabilities of multistable structures for enhanced performance and versatility.

## REFERENCES

- [1] Y. Forterre, J. M. Skotheim, J. Dumais, and L. Mahadevan, "How the venus flytrap snaps," *Nature*, vol. 433, no. 7024, pp. 421–425, 2005.
- [2] M. Smith, G. Yanega, and A. Ruina, "Elastic instability model of rapid beak closure in hummingbirds," *J. Theor. Biol.*, vol. 282, no. 1, pp. 41–51, 2011.
- [3] J. Kaufmann, P. Bhovad, and S. Li, "Harnessing the multistability of kresling origami for reconfigurable articulation in soft robotic arms," *Soft Robot.*, vol. 9, no. 2, pp. 212–223, 2022.
- [4] S. Wu, Q. Ze, J. Dai, N. Udupi, G. H. Paulino, and R. Zhao, "Stretchable origami robotic arm with omnidirectional bending and twisting," *Proc. Nat. Acad. Sci. USA*, vol. 118, no. 36, 2021, Art. no. e2110023118.
- [5] Y. Chi, Y. Li, Y. Zhao, Y. Hong, Y. Tang, and J. Yin, "Bistable and multi-stable actuators for soft robots: Structures, materials, and functionalities," *Adv. Mater.*, vol. 34, no. 19, 2022, Art. no. 2110384.
- [6] Y. Cao, M. Derakhshani, Y. Fang, G. Huang, and C. Cao, "Bistable structures for advanced functional systems," *Adv. Funct. Mater.*, vol. 31, no. 45, 2021, Art. no. 2106231.
- [7] S. Wu, G. L. Baker, J. Yin, and Y. Zhu, "Fast thermal actuators for soft robotics," *Soft Robot.*, vol. 9, no. 6, pp. 1031–1039, 2022.
- [8] J. T. Overvelde, T. Kloek, J. J. D'haen, and K. Bertoldi, "Amplifying the response of soft actuators by harnessing snap-through instabilities," *Proc. Nat. Acad. Sci. USA*, vol. 112, no. 35, pp. 10863–10868, 2015.
- [9] Y. Tang et al., "Leveraging elastic instabilities for amplified performance: Spine-inspired high-speed and high-force soft robots," *Sci. Adv.*, vol. 6, no. 19, 2020, Art. no. eaaz6912.
- [10] Z. Zhakypov, K. Mori, K. Hosoda, and J. Paik, "Designing minimal and scalable insect-inspired multi-locomotion millirobots," *Nature*, vol. 571, no. 7765, pp. 381–386, 2019.
- [11] D. K. Patel et al., "Highly dynamic bistable soft actuator for reconfigurable multimodal soft robots," *Adv. Mater. Technol.*, vol. 8, no. 2, 2023, Art. no. 2201259.
- [12] Y. Chi, Y. Hong, Y. Zhao, Y. Li, and J. Yin, "Snapping for high-speed and high-efficient butterfly stroke-like soft swimmer," *Sci. Adv.*, vol. 8, no. 46, 2022, Art. no. eadd3788.
- [13] T. Bambrick, A. Viquerat, and R. Siddall, "Does bistability improve swimming performance in robotic fish?," *Adv. Intell. Syst.*, 2024, Art. no. 2300748.
- [14] E. Lerner, H. Zhang, and J. Zhao, "Design and experimentation of a variable stiffness bistable gripper," in *Proc. IEEE/RSJ Int. Conf. Intell. Robots Syst.*, 2020, pp. 9925–9931.
- [15] H. Hsiao, J. Sun, H. Zhang, and J. Zhao, "A mechanically intelligent and passive gripper for aerial perching and grasping," *IEEE/ASME Trans. Mechatronics*, vol. 27, no. 6, pp. 5243–5253, Dec. 2022.
- [16] C. Geckeler and S. Mintchev, "Bistable helical origami gripper for sensor placement on branches," *Adv. Intell. Syst.*, vol. 4, no. 10, 2022, Art. no. 2200087.
- [17] S. Spiegel, J. Sun, and J. Zhao, "A shape-changing wheeling and jumping robot using tensegrity wheels and bistable mechanism," *IEEE/ASME Trans. Mechatronics*, vol. 28, no. 4, pp. 2073–2082, Aug. 2023.
- [18] J. A. Faber, A. F. Arrieta, and A. R. Studart, "Bioinspired spring origami," *Science*, vol. 359, no. 6382, pp. 1386–1391, 2018.
- [19] H. Zhang, E. Lerner, B. Cheng, and J. Zhao, "Compliant bistable grippers enable passive perching for micro aerial vehicles," *IEEE/ASME Trans. Mechatronics*, vol. 26, no. 5, pp. 2316–2326, Oct. 2021.
- [20] Y. Jiang et al., "Reprogrammable bistable actuators for multimodal, fast, and ultrasensitive grasping," *IEEE/ASME Trans. Mechatronics*, vol. 29, no. 2, pp. 984–994, Apr. 2024.
- [21] J. Sun, B. Tighe, and J. Zhao, "Tuning the energy landscape of soft robots for fast and strong motion," in *Proc. IEEE Int. Conf. Robot. Automat.*, 2020, pp. 10082–10088.
- [22] Y. Liu et al., "A soft and bistable gripper with adjustable energy barrier for fast capture in space," *Soft Robot.*, vol. 10, no. 1, pp. 77–87, 2023.
- [23] L. Jiang et al., "Electroactive soft bistable actuator with adjustable energy barrier and stiffness," *IEEE Trans. Robot.*, vol. 40, pp. 472–482, 2023.
- [24] A. Pal and M. Sitti, "Programmable mechanical devices through magnetically tunable bistable elements," *Proc. Nat. Acad. Sci. USA*, vol. 120, no. 15, 2023, Art. no. e2212489120.
- [25] Z. Xiong, Y. Su, and H. Lipson, "Fast untethered soft robotic crawler with elastic instability," in *Proc. IEEE Int. Conf. Robot. Automat.*, 2023, pp. 2606–2612.
- [26] Z. Xiong, Z. Guo, L. Yuan, Y. Su, Y. Liu, and H. Lipson, "Rapid grasping of fabric using bionic soft grippers with elastic instability," in *Proc. IEEE/RSJ Int. Conf. Intell. Robots Syst.*, 2023, pp. 6449–6455.
- [27] Y. Chi, Y. Tang, H. Liu, and J. Yin, "Leveraging monostable and bistable pre-curved bilayer actuators for high-performance multitask soft robots," *Adv. Mater. Technol.*, vol. 5, no. 9, 2020, Art. no. 2000370.
- [28] L. Zhou, A. E. Marras, H. J. Su, and C. E. Castro, "Direct design of an energy landscape with bistable DNA origami mechanisms," *Nano Lett.*, vol. 15, no. 3, pp. 1815–1821, 2015.
- [29] A. F. Arrieta, V. Van Gemmeren, A. J. Anderson, and P. M. Weaver, "Dynamics and control of twisting bi-stable structures," *Smart Mater. Structures*, vol. 27, no. 2, 2018, Art. no. 025006.
- [30] T. Chen, O. R. Bilal, K. Shea, and C. Daraio, "Harnessing bistability for directional propulsion of soft, untethered robots," *Proc. Nat. Acad. Sci. USA*, vol. 115, no. 22, pp. 5698–5702, 2018.
- [31] Y. Zhang, Y. Jiao, J. Wu, Y. Ma, and X. Feng, "Configurations evolution of a buckled ribbon in response to out-of-plane loading," *Extreme Mechanics Lett.*, vol. 34, 2020, Art. no. 100604.



**Zhe Chen** (Graduate Student Member, IEEE) received the B.E. degree in mechanical engineering from Jilin University, Changchun, China, in 2013, and the M.E. degree in mechanical engineering from the Huazhong University of Science and Technology, Wuhan, China, in 2019. He is currently working toward the Ph.D. degree in mechanical engineering with Colorado State University, Fort Collins, CO, USA.

His current research interests include reconfigurable robot and shape morphing structures.



**Jiefeng Sun** (Member, IEEE) received the B.S. degree in mechanical engineering from the Lanzhou University of Technology, Lanzhou, China, in 2014, the M.S. degree in mechanical engineering from the Dalian University of Technology, Dalian, China, in 2017, and the Ph.D. degree in mechanical engineering from Colorado State University, Fort Collins, CO, USA, in 2022.

He is currently an Assistant Professor with Arizona State University, Tempe, AZ, USA. His current research interests include artificial muscle, soft robots, and reconfigurable robots.



**Jianguo Zhao** (Member, IEEE) received the B.E. degree in mechanical engineering from the Harbin Institute of Technology, Harbin, China, in 2005, the M.E. degree in mechatronic engineering from Shenzhen Graduate School, Harbin Institute of Technology, Shenzhen, China, in 2007, and the Ph.D. degree in electrical engineering from Michigan State University, East Lansing, Michigan, USA, in 2015.

He is currently an Associate Professor with Colorado State University, Fort Collins, CO, USA, and the Director of Adaptive Robotics Lab. His research interests include soft robots, flying robots, and reconfigurable robots.

Dr. Zhao currently serves as a Technical Editor for IEEE/ASME TRANSACTIONS ON MECHATRONICS.